Dalton Transactions

Accepted Manuscript

ROYAL SOCIETY OF CHEMISTRY

www.rsc.org/dalton

Dalton Transactions

Guidelines to Referees

Communications & Papers

The international journal for inorganic, organometallic and bioinorganic chemistry

http://www.rsc.org/dalton

Dalton Transactions wishes to encourage high quality articles reporting exciting new developments in inorganic chemistry.

For an article to be accepted, it must report new, high-quality research and make a significant contribution to the field.

Manuscripts which describe purely physical, crystallographic or computational studies must include the clear relevance of the work to the broad inorganic chemistry readership of *Dalton Transactions*.

Communications must report chemistry of sufficient importance and impact to justify preliminary publication. **Papers** should report more complete studies.

***Dalton Transactions* Impact Factor is 4.19** (2014 Journal Citation Reports®)

Routine or unnecessarily fragmented work, however competently researched and reported, should not be recommended for publication.

Thank you very much for your assistance in evaluating this manuscript

Dr Andrew Shore (dalton@rsc.org)
Royal Society of Chemistry
Editor, *Dalton Transactions*

Professor Philip Mountford
University of Oxford
Chair, *Dalton Transactions* Editorial Board

General Guidance (for further details, see the RSC Refereeing Procedure and Policy)

When preparing your report, please:

- Comment on the **originality**, **importance**, **impact** and **scientific reliability** of the work
- State clearly whether you would like to see the paper accepted or rejected and give detailed comments (with references, as appropriate) that will help both the Editor to make a decision on the paper and the authors to improve it

Please inform the Editor if:

- There is a conflict of interest
- There is a significant part of the work which you are not able to referee with confidence
- If the work, or a significant part of the work, has previously been published, including online publication (*e.g.* on a preprint server/open access server)
- You believe the work, or a significant part of the work, is currently submitted elsewhere
- The work represents part of an unduly fragmented investigation

Graphical Abstract

The hollow porous Ni/SnO_2 hybrid composites exhibit the superior properties with the features of strong absorption, thin thickness, broad bandwidth and light weight.

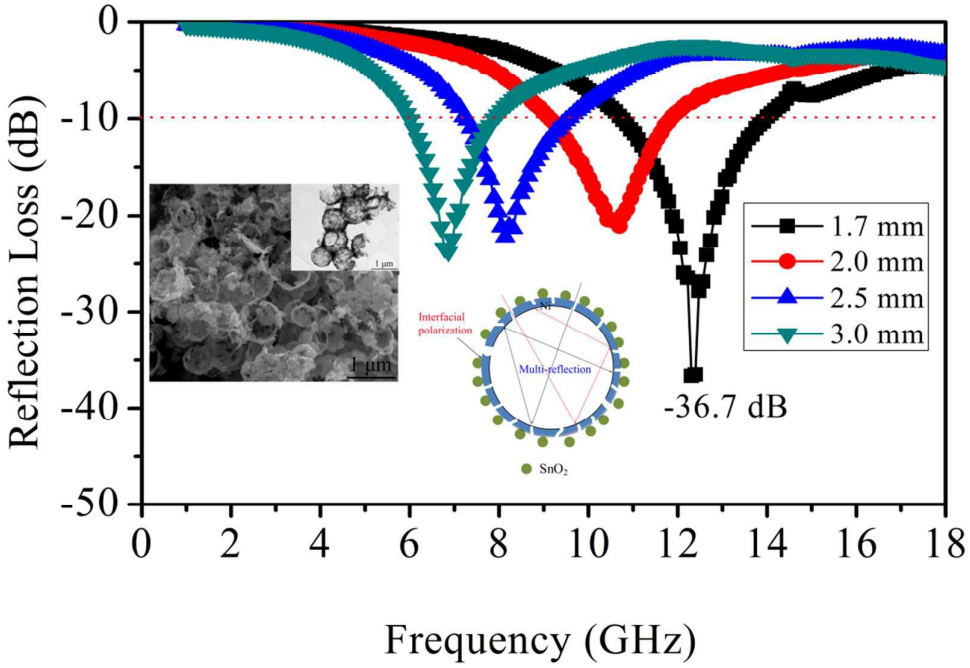

Corrosive synthesis and enhanced electromagnetic absorption properties of hollow porous Ni/SnO_2 hybrids

Biao Zhao [a], Wanyu Zhao [a], Gang Shao [a] *, Bingbing Fan [a], Rui Zhang [a, b] *

Received (in XXX, XXX) Xth XXXXXXXXX 20XX, Accepted Xth XXXXXXXXX 20XX
DOI: 10.1039/c000000x

ABSTRACT: In this work, the novel porous hollow Ni/SnO_2 hybrids were prepared by a facile and flexible two-step approach composed of solution reduction and subsequently reaction-induced acid corrosion. In our protocol, it can be found that the hydrothermal temperature plays a vital influence on the phase crystal and morphology of Ni/SnO_2 hybrids. Notably, the Ni microspheres might be completely corroded in the hydrothermal process at 220 °C. The complex permittivity and permeability of Ni/SnO_2 hybrids–paraffin wax composite were measured based on a vector network analyzer in the frequency of 1–18 GHz. Electromagnetic absorption properties of samples were evaluated by transmission line theory. Ni/SnO_2 hybrid composites exhibit superior electromagnetic absorption properties in comparison with pristine Ni microspheres. The outstanding electromagnetic absorption performances can be obtained for the hollow porous Ni/SnO_2 hybrid prepared at 200 °C. The minimum reflection loss is −36.7 dB at 12.3 GHz and effective electromagnetic wave absorption band (RL< -10 dB, 90% microwave attenuation) was in the frequency range of 10.6–14.0 GHz with the thin thickness of 1.7 mm. The excellent electromagnetic absorption properties were assigned to the improved impedance match, more interfacial polarization and unique hollow porous structures, which can result in microwave multi-reflection and scattering. This novel hollow porous hybrid is an attractive candidate for new types of high performance electromagnetic wave absorbing materials, which satisfies the current requirements of electromagnetic absorbing materials of wide-band absorption, high-efficiency absorption capability, thin thickness and lightweight.

1. Introduction

In past decades, electromagnetic absorbing materials have drawn more and more attentions to absorb or at least dissipate unwanted electromagnetic wave, which can not only harm the human body but also play a negative influence on the performance of electrical circuits. [1-4] The electromagnetic absorption materials can absorb microwaves effectively and convert electromagnetic energy into heat energy or other styles of energy. [5, 6] Nowadays, the ideal microwave absorption material should meet the features of small thickness, lightweight, wide-band, and high efficiency absorption. [7-9]

The electromagnetic absorption properties are mainly correlated with the complex permittivity, complex permeability, electromagnetic wave impedance match as well as the microstructures. [10] Among the electromagnetic wave absorbers, metallic nickel particles with relatively large permeability associated with low cost have been extensively investigated. [11-13] However, Ni would induce eddy current effect by microwave in GHz range due to its high conductivity. The eddy current gives rise to impedance mismatching between the absorber and space, which would cause more microwave reflection and less microwave absorption. To alleviate this issue, an effective strategy is to prepare complex architectures of Ni or prepared Ni-based composite materials. Extensive studies have been performed on the Ni-based composites. For example, Ni/SnO_2 composite, [14] carbon-coated Ni, [15] PS@PPy@Ni, [16] Ni/Polypyrrole, [17] Ni/polyaniline, [18] and Ni/ZnS [19] exhibit the better microwave absorption properties than the individual raw Ni or other materials. Therefore, the electromagnetic wave absorption capabilities of Ni materials could be significantly improved after mixing with inorganic and nonmagnetic materials.

As an n-type wide-bandgap (E_g = 3.6 eV) semiconductor, SnO_2 is one of the most intensively studied materials, which are potentially used in a variety of applications containing chemical, electronic, optical, and mechanical fields, owing to its relatively high conductivity, photoluminescence, chemical stability, and gas sensitivity.[20-23] Recently, the researches on microwave absorption and dielectric property of SnO_2 based-materials have also been reported. [24-26] Chen and co-workers prepared porous Fe_3O_4/SnO_2 core/shell nanorods, which exhibit excellent microwave absorption properties. The authors attributed outstanding microwave absorption properties to synergetic effects between the magnetic loss and the dielectric loss as well as the unique core-shell structures.[24] Liu et al. synthesized double-shelled Fe_3O_4@SnO_2 yolk−shell microspheres, which exhibit

significantly enhanced electromagnetic absorption properties compared with the pure Fe_3O_4 particles.[25] Mishra et al. fabricated the SnO_2@RGO composites and investigated their microwave shielding performance at the X-band (8.2–12.4 GHz) range.[26] In our previous literatures,[14, 27] the electromagnetic absorption properties of Ni microspheres are obviously improved after coating with SnO_2 nanoparticles.

From the above results, it can be inferred that introduction of SnO_2 into the composite materials can enhance the microwave absorption properties. However, as far as we know, the reports about electromagnetic properties of Ni/SnO_2 hybrids are scarcely found in the published papers, let alone for the hollow porous Ni/SnO_2 hybrids. In previous literatures, plentiful methods were utilized to prepare Ni/SnO_2 composites. For example, a chloride-based inorganic sol–gel route was used for preparing Ni doped SnO_2 sol. [28] Haq et al. reported that Ni–SnO_2 composite coatings were deposited onto steel substrates by the electrodeposition method from electrolyte solutions. [29] Lavanya et al. synthesized Ni doped SnO_2 nanoparticles by a simple microwave irradiation (2.45 GHz) method. [30] These methods need complex process and more cost. In this work, the hollow porous Ni/SnO_2 hybrids were successfully synthesized by a two-step process including solution reduction and subsequently chemical conversion-induced H^+ corrosion. The SnO_2 nanoparticles are decorated on the hollow porous skeletons, which can improve impedance match, dielectric loss, and induce interfacial polarization between SnO_2 with Ni. Moreover, the hollow porous can tune the complex permittivity of hybrids and cause multiple reflection in the confine space. The hollow porous Ni/SnO_2 hybrids exhibit outstanding microwave absorption properties with the attributes of high efficiency absorption, thin thickness, light weight and broad bandwidth, which can meet current requirement of electromagnetic absorbing materials. From this view, this is a competitive work.

2. Experimental Section

All the reagents were of commercial available and used without any further purification. Hollow porous Ni/SnO_2 hybrids were obtained by means of a two-step approach.

2.1 Preparation of Ni microspheres

Ni microspheres were synthesized by the solution reduction method according to our earlier reports.[14, 19, 27, 31, 32] Briefly, 1.2 g $NiCl_2 \cdot 6H_2O$, 0.3 g trisodium citrate and 3.0 g sodium acetate were dissolved in 60 ml 1,2-propanediol. Subsequently, $N_2H_4 \cdot H_2O$ (6 ml) was introduced into the solution. The mixture was stirred intensely for 30 min and then added into a Teflon-lined stainless steel autoclave. The autoclave was maintained at 140 ºC for 15 h. The final products were collected from the solution. The final products were dried at 60 ºC for 12 h in vacuum.

2.2 Synthesis of hollow porous Ni/SnO_2 nanocomposites

The hollow porous Ni/SnO_2 nanocomposites were prepared through a corroding approach. Typically, 0.05 g of as-obtained Ni microspheres was dispersed in a mixture of 1,2-propanediol (30 ml) and distilled water (30 ml). Then, 0.45 g $SnCl_2 \cdot 2H_2O$ was added into the above solution. Then the mixture was transferred into a Teflon-lined stainless and kept 200 ºC for 15 h. The product was filtered out and washed with ethanol and distilled water. The obtained products were dried at 60 ºC overnight in vacuum. Three Ni/SnO_2 composites were prepared at 180 ºC, 200 ºC and 220 ºC, denoted as Ni/SnO_2-180, Ni/SnO_2-200 and Ni/SnO_2-220, respectively.

2.3 Characterization

The phase and purity of the product was characterized by powder X-ray diffraction (XRD) analyses (XD-3, Cu Kα radiation, λ =1.54178 Å. Beijing Purkinje General Instrument Co. Ltd). The morphologies of the as-synthesized nickel products were observed with field emission scanning electron microscopy (FE-SEM, JEOL JSM-7001F) and transmission electron microscope (TEM, FEI Tecnai 12). The element composition was performed by an energy dispersive X-ray spectroscopy (EDS, Oxford Instruments) associated with SEM. Nitrogen adsorption−desorption isotherms were conduted on a Quantachrome AsiQM0000-3, and the specific surface area was measured by the Brunauer−Emmett−Teller (BET) method. The static magnetic properties of the as-obtained hollow porous

Ni/SnO_2 composites were performed by a Lake Shore 7404 vibrating sample magnetometer (VSM) at room temperature. The products were blended with paraffin wax and formed into ring-shaped samples (7 mm in outer diameter, 3.04 mm in inner diameter) for electromagnetic absorption measurement. The electromagnetic parameters of the composite samples with 50 wt% of the hollow Ni/SnO_2 were measured in the 1–18 GHz range using an Agilent N5244A vector network analyzer.

3. Results and discussion

The phase compositions and structures of the fabricated samples were characterized by powder XRD and the recorded patterns are presented in Fig. 1. Fig.1a shows the typical XRD pattern of pristine Ni microspheres. All the diffraction peaks can be well assigned to face-centered cubic Ni (JCPDS card No. 04-0850). When the hydrothermal temperature is 180 °C, the XRD peaks of obtained-products can be indexed to Ni phase (indicated by triangles) compared with the data in JCPDs No.04-0850. The other peaks indicated by solid circles corresponding to tetragonal rutile SnO_2 (JCPDs No. 41-1445) are also observed, suggesting that the composites were composed of Ni and SnO_2 (Fig. 1b). With increasing the reaction temperatures to 200 °C (Fig.1c), it is noting that the intensity of diffraction peaks of the Ni phase are weakened in comparison with the raw Ni microspheres, while the diffraction peaks of SnO_2 become stronger. Notably, at 220 °C (Fig.1d), there are main peaks of SnO_2 and the diffraction peaks of Ni phase are hardly observed, which implies that the Ni particles might transform into Ni^{2+} ion in this system at elevated temperatures.

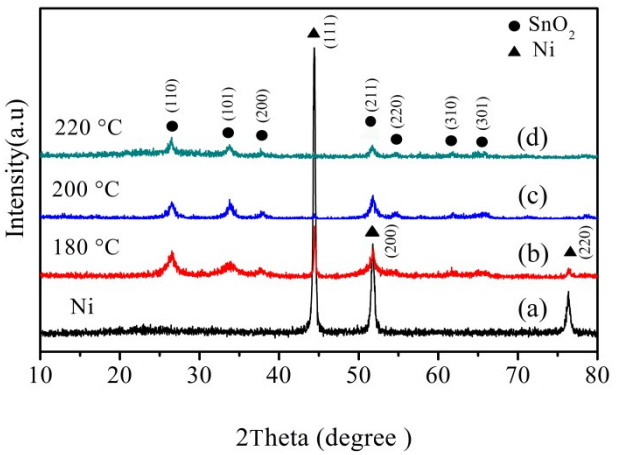

Fig. 1 XRD patterns of (a) pristine Ni microspheres, (b-d) Ni/SnO_2 composites prepared at 180 °C, 200 °C and 220 °C, respectively.

To reveal the morphologies of the as-received composites, SEM measurements were performed and the results were shown in Fig.2. Fig. 2a presents the FESEM image of pure Ni microspheres. It can be obviously seen that the Ni microspheres have a relatively smooth surface with an average diameter of 0.9 μm. Fig. 2(b,c) show the images of Ni/SnO_2 composite prepared at 200 °C using the $SnCl_2{\cdot}2H_2O$ as starting reagent, which indicate that these particles should be hollow or porous inside of the body. Furthermore, large number of small nanoparticles can be observed around the hollow Ni powders. The EDS analysis of as-synthesized Ni/SnO_2 composite indicates the presence of Ni, O, and Sn elements, respectively (Fig.2d). The C peaks come from electronic conductive substrate to support the measured sample. From the XRD and SEM results, it can be deduced that the Ni microspheres are dissolved or etched to form hollow of porous structure in the hydrothermal reaction process. Meanwhile, SnO_2 nanoparticles were formed around hollow Ni particles by oxidization of the Sn^{2+}. The formation mechanism of hollow porous Ni/SnO_2 composite will be further discussed in details.

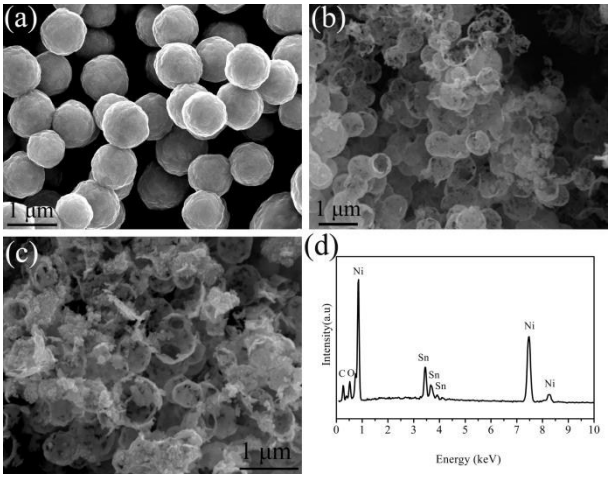

Fig. 2 (a) FESEM image of raw Ni microspheres; (b,c) FESEM images of hollow porous Ni/SnO_2 composite obtained at 200 °C and (d) corresponding EDS curve of Ni/SnO_2 composite.

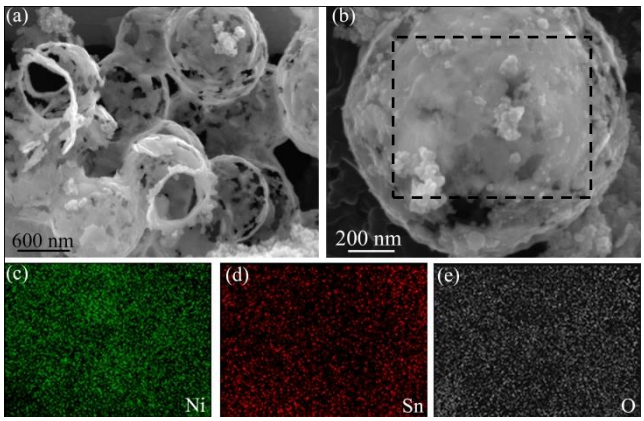

Fig.3 (a,b) The different magnification FESEM images of hollow Ni/SnO_2 hybrids; (c-e) the element mapping of Ni, Sn and O, respectively.

To obtain more information of microstructure of Ni/SnO_2 hybrids, the high magnification FESEM images and corresponding elemental mapping were shown in Fig.3. From the Fig.3(a,b), one can note that the Ni/SnO_2 hybrids possess the characteristic of hollow porous structure. Moreover, as shown in Fig.3(c-e), the distribution of elements (Ni, Sn, O) is uniform, which signified that the nanoparticles SnO_2 were deposited on the hollow Ni skeletons evenly.

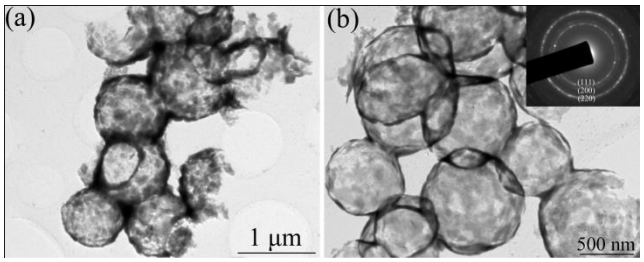

Fig. 4 TEM images of hollow Ni/SnO_2 composite prepared at 200 °C with different magnifications. Inset of Fig.3b is the SAED pattern of hollow Ni/SnO_2 hybrids.

To further validate the hollow porous structure, the TEM technique was also used to characterize this hollow Ni/SnO_2 composite. Fig. 4a and 4b exhibit different magnification TEM images of the hollow Ni/SnO_2 composites. The strong contrast between the pale center and the dark edge shown in the TEM image confirms the hollow structure of the composite microspheres, which is in accordance with the SEM results. It is noteworthy that no dispersed nanoparticles could be seen from the TEM images, which might be attributed to the ultrasonic dispersion before TEM observation. It indicates that the SnO_2 nanoparticles were only deposited on the hollow Ni microspheres rather than formation of the chemical bond between Ni and SnO_2. The selected-area electron diffraction (SAED) pattern shown in the upper right corner of Fig. 4b gives clear concentric rings, which can be indexed as the (111), (200), (220) planes of Ni. It also validates that the hollow skeleton is natural attributes of Ni crystal. To further confirm the microstructure of the hollow porous Ni/SnO_2 hybrids, nitrogen absorption–desorption measurements were carried out to study the porosity and surface area. Fig. S1 depicts the nitrogen absorption–desorption isotherms and the corresponding pore size distribution of hollow porous Ni/SnO_2 hybrids. The isotherms can be assigned to type IV with a distinct hysteresis loop, indicating the formation of mesoporous structures. The distribution of pore size (inset in Fig. S1) was calculated through the Barrett–Joyner–Halenda (BJH) method. From the distribution pattern, the dominant pore diameter is about 3-10 nm in the resultant product. The BET surface area of the hollow porous Ni/SnO_2 spheres was 6.4 m^2g^{-1}.

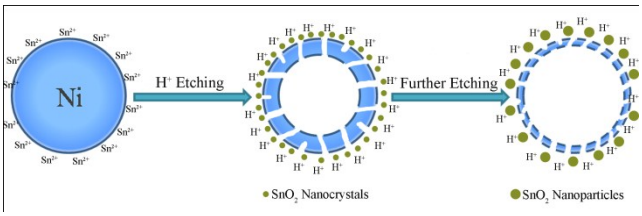

Fig. 5 Schematic illustration of the formation mechanism for hollow porous Ni/SnO_2 composite

According to the above analysis, a plausible mechanism of the formation of hollow porous was proposed, which can be attributed to chemical reaction-induced H^+ corrosion (Fig. 5). Firstly, solid Ni microspheres were dispersed in the mixture solution containing a large number of Sn^{2+} ions. When the system was placed at hydrothermal temperature of 200 °C, the Sn(II) was oxidized to Sn(IV), which can be performed by dissolving oxygen in the precursor solution. The oxidation into Sn(IV) is necessary for the synthesis of SnO_2. [23] Meanwhile, the H^+ ion was produced during the reaction process. Thus Ni microspheres were corroded by the H^+ ion to form hollow or porous Ni particles and the freshly SnO_2 nanocrystals were deposited on the Ni framework. The thickness of Ni frameworks become thin and more broken hollow Ni particles were generated with further etching. Moreover, numerous small SnO_2 crystallites first nucleate under hydrothermal conditions and then gradually aggregate nanoparticles to minimize their surface energies. Therefore, the hollow porous Ni/SnO_2 were obtained (Fig. 2b,c). From the SEM and TEM images, it can be found that the porous hollow Ni skeletons were successfully synthesized by the acid of H^+ corrosion. The surfaces are firstly corroded by the existence of H^+ ions. Then, the H^+ ions travel into the interior parts of Ni microspheres and reacted with these interior Ni parts, which is due to the fact that these interior Ni parts possess relatively high surface energy. This process is very similar with the Ostwald ripening process.[33, 34] During this ripening process, the inner crystallites would dissolve and transfer out, producing hollow structures. The overall reaction can be described by the following equations: [35, 36]

$$2Sn^{2+} + 2H_2O + O_2 \rightarrow 2SnO_2 + 4H^+ \quad (1)$$

$$2H^+ + Ni \rightarrow Ni^{2+} + H_2\uparrow \quad (2)$$

The corrosive performances of Ni were found to be sensitive to hydrothermal temperatures. We have systematically investigated this system with reaction temperatures in the range of 180–220 °C and the SEM images of the products obtained at different reaction temperatures are shown in Fig. 6. It can be seen that for the Ni microspheres corroded at temperature of 180 °C, many pinning corroding hollow Ni microspheres and un-corroded Ni coexisted in the products, which indicates the occurrence of general corrosion. Moreover, lots of SnO_2 nanoparticles are depositing on the Ni microspheres (Fig.6a,b). With increasing of the reaction temperature to 200 °C, the obtained products are mainly composed of hollow porous Ni skeletons together with plentiful nanoparticles (Fig. 6c,d). Further observation, it can be found that the thickness of Ni skeletons prepared at 200 °C was thinner than those of Ni skeletons obtained at 180 °C. With a further increase in the reaction temperature to 220 °C, it was fascinating that the hollow porous Ni skeletons were disappeared, which means the Ni microspheres might be completely converted into Ni^{2+} by the H^+ corrosion at high temperatures, and the product was mainly composed of aggregated SnO_2 particles (Fig.6e,f). Based on above results, it is clear that the hollow porous Ni/SnO_2 hybrids are formed only when reaction temperature is in the range 180–200 °C.

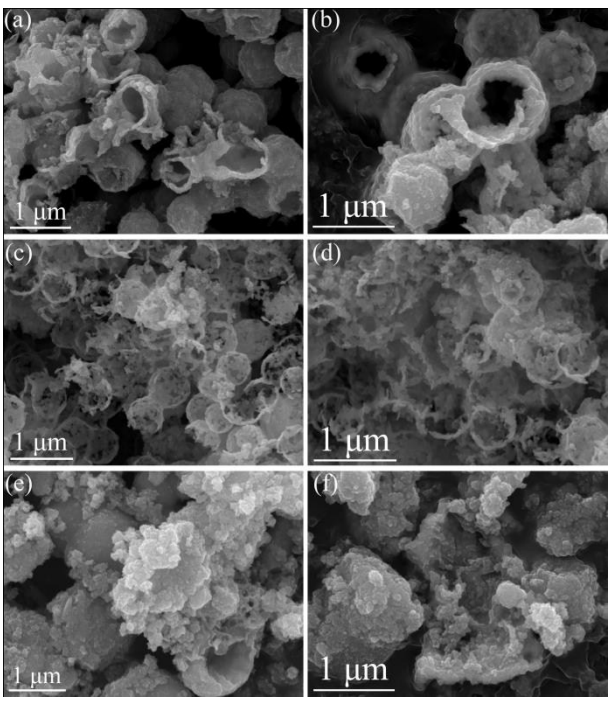

Fig. 6 FESEM images of the Ni/SnO_2 samples obtained by corroding the Ni microspheres at temperatures of (a,b) 180 °C, (c,d) 200 °C, (e,f) 220 °C.

The magnetic properties of Ni/SnO_2 hybrids were studied at room temperature using a vibrating sample magnetometer (Fig.7). However, plot of Ni/SnO_2-220 hybrid exhibits nonmagnetic behavior as saturation magnetization and coercivity are nearly zero. This is due to the nearly completely corrosion of Ni skeletons at high temperature. The Ni/SnO_2-180 and Ni/SnO_2-200 exhibit typical ferromagnetic hysteresis loops, caused by the presence of metallic Ni particles. The saturation magnetization (M_S) of Ni/SnO_2-180 and Ni/SnO_2-200 is 20.6 and 8.9 emu g^{-1}, respectively, which are lower than that of bulk Ni (ca. 55.2 emu g^{-1}).[11] The low M_S of the as-prepared Ni/SnO_2 samples is mainly attributed to the presence of nonmagnetic SnO_2. It is noting that the saturation magnetization of Ni/SnO_2 hybrids is prone to decrease with elevating hydrothermal temperature. This is due to the decease of SnO_2 amounts with the increase of hydrothermal temperature. The magnetic properties of Ni/SnO_2 hybrids can induce magnetic loss under the alternated electromagnetic field.

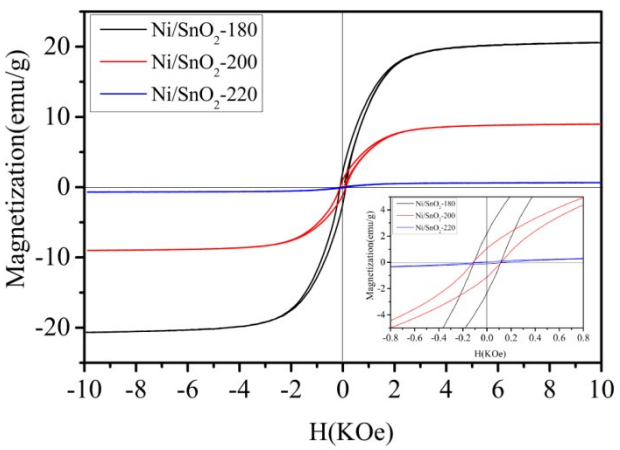

Fig.7 Magnetic hysteresis loops of Ni/SnO_2-180, Ni/SnO_2-200, and Ni/SnO_2-220 samples at 300 K. Inset shows the corresponding magnified hysteresis loops at low applied magnetic fields.

The electromagnetic parameters (complex permittivity, $\varepsilon_r = \varepsilon' - j\varepsilon''$, and complex permeability, $\mu_r = \mu' - j\mu''$) of the Ni/SnO_2 composites in the paraffin matrix were measured in the range 1–18 GHz to investigate the electromagnetic absorbing properties of Ni/SnO_2 composites. It is well known that the imaginary permittivity (ε″) and the imaginary permeability (μ″) symbolize the storage ability of electric and magnetic energy, while real permittivity (ε′) and the real permeability (μ′) signify the dissipation ability of electric and magnetic energy.[37] Fig.8 shows the frequency dependence of complex permeability and complex permittivity for the Ni/SnO_2 hybrids. It was observed that over the entire frequency range, ε′ values remained almost constant (Fig.8a). Notably, the ε′ values of Ni/SnO_2-200 sample were higher than other two Ni/SnO_2 samples. It indicates better energy storage and polarization, which is attributed to the more porous sites and thin Ni skeletons. Fig. 8b shows the imaginary parts (ε″) of Ni/SnO_2 hybrids. From the Fig.8b, one can see that Ni/SnO_2-200 sample shows the highest ε″ values in the three hybrid products, which indicates the highest dissipation ability of electric loss for the Ni/SnO_2-200 sample. Notably, the three hybrid composites exhibit multiple peaks on the imaginary part (ε″) curves, symbolizing a resonance behavior, which is supposed to happen when the absorbing materials are highly conductive and skin effect is dominant. [38] Furthermore, as to the Ni/SnO_2-200 and Ni/SnO_2-180 hybrid composites, these phenomena are clearly observed, which is also named the nonlinear resonant behaviors. [39] It mainly results from the synergetic effect of the hollow porous Ni frameworks, the interfaces between Ni and dielectric SnO_2 materials. According to the free electron theory, [40, 41] $\varepsilon'' \approx 1/\pi\varepsilon_0\rho f$, where ρ is the resistivity. The conductivity of the Ni/SnO_2-200 samples is higher than those of other Ni/SnO_2 hybrid samples. For the Ni/SnO_2-200 samples, the thin and hollow porous Ni skeletons could link with each other and a continuous microcurrent gradually generates, which would lead to low electric resistivity and induce conduction and electric loss. [42] Otherwise, the SnO_2 nanoparticles deposited on the Ni skeletons can induce dipolar and oriented polarization under alternating electromagnetic field.[43]

The real part (μ′) and imaginary part (μ″) of relative complex permeability of Ni/SnO_2 hybrid composites are shown in Fig. 8c–d. For the Ni/SnO_2-200 and Ni/SnO_2-180 samples, the real part (μ′) of complex permeability present a similar frequency dependence behavior and the values decrease slowly with the increase of frequency. From Fig.8d, one can note that Ni/SnO_2-200 sample exhibits the largest μ″ values, which means the high attenuation capabilities of magnetic loss in the three Ni/SnO_2 composites. Furthermore, for the Ni/SnO_2-200 and Ni/SnO_2-180 samples, the μ″ values show the multiple peaks, which indicate the resonance behaviors. In general, the resonance could be attributed to natural resonance at the low frequency,[44] while other resonances could be due to exchange resonances at the high frequency. [45, 46] Interestingly, for the Ni/SnO_2-220 sample, the complex permeability (μ′~1, μ″~0) can be neglected due to that the Ni particles can be corroded absolutely at high temperature, which are also in good accordance with XRD and SEM observations. The porous hollow structure can effectively modulate the permittivity of magnetic particles.[36, 47] Meanwhile, hollow porous materials are helpful for suppressing the eddy current loss of metallic magnets and maintaining high permeability at GHz range. [48] Combing decrease of permittivity and retention of high permeability, benefits impedance match, which is available for enhancement of electromagnetic absorption properties.

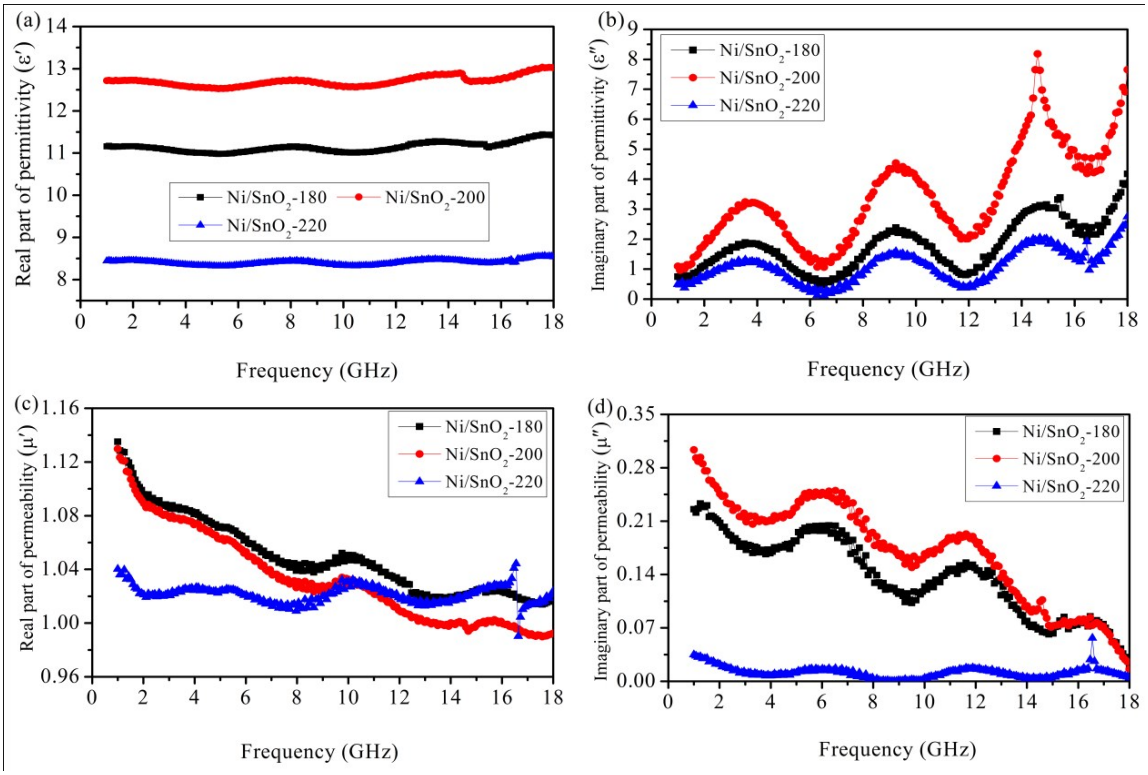

Fig. 8 Frequency dependence of (a) the real part (ε′) and (b) imaginary part (ε″) of the complex permittivity, (c) the real part (μ′) and (d) imaginary part (μ″) of the complex permeability of the Ni/SnO_2-180, Ni/SnO_2-200 and the Ni/SnO_2-220.

Generally, the permittivity behaviors of electromagnetic absorption materials can be explained by the relaxation process. The relaxation process can be described by the Cole–Cole semicircle. According to the Debye dipolar relaxation,[49-51] the relationship between ε′ and ε″ can be deduced

$$\left(\varepsilon' - \varepsilon_\infty\right)^2 + \left(\varepsilon''\right)^2 = \left(\varepsilon_s - \varepsilon_\infty\right)^2 \quad (3)$$

In which ε_∞ , ε_s are the relative dielectric permittivity at the high-frequency limit and static permittivity, respectively. Thus, the plot of ε′ versus ε″ would be a single semicircle, in general, denoted as the Cole–Cole semicircle. [52] Each semicircle corresponds to one Debye relaxation process. Fig. S2(a-c) exhibit

the profiles of ε′ as function of ε″ for the Ni/SnO_2 paraffin composites. It is evident that six semicircles for Ni/SnO_2-200 were observed, suggesting the presence of some semicircles. It indicates that there are several relaxation processes in Ni/SnO_2-200 hybrid composite. It demonstrates that the presence of hollow porous Ni skeleton promotes the intensity of the Debye dipolar relaxation process. Interfaces between hollow skeletons and SnO_2 particles are the cause of Debye dipolar relaxation processes, which are beneficial for the enhancement of microwave absorption. As previously discussed above, the free electron theory ($\varepsilon'' \approx 1/\pi\varepsilon_0\rho f$) uncovers that the ε″ values of the dielectric constant are proportional to the absorber conductance. According to our earlier paper, [14] pure Ni possesses high electronic conductivity and the strong dielectric loss of Ni. However, when the surfaces of Ni particles are irradiated by an electromagnetic wave, the high conductivity of metal Ni would lead to the occurrence of a significant skin effect. [11, 12] High ε″ for Ni or low ε″ for SnO_2 particles (Fig. 8b) would lower impedance matching [53] of electromagnetic absorbing materials. It is the reason why pristine Ni and SnO_2 particles present very weak electromagnetic absorption properties, as shown in Fig. 9. In current work, the new composites were designed with appropriate contents of hollow porous Ni and SnO_2 particles, which make absorbers meet the requirements of impedance matching.

Electromagnetic attenuation is one of vital points for an excellent electromagnetic absorber. The attenuation constant α determines the absorption properties of absorbing material. According to transmission line theory and electromagnetic wave propagation constant, the α can be described by: [54, 55]

$$\alpha = \frac{\sqrt{2}\pi f}{c} \times \sqrt{(\mu''\varepsilon'' - \mu'\varepsilon') + \sqrt{(\mu''\varepsilon'' - \mu'\varepsilon')^2 + (\mu'\varepsilon'' + \mu''\varepsilon')^2}} \quad (4)$$

In which f , c are the frequency of the electromagnetic wave and is the velocity of light, respectively. As shown in Fig.S3, the dependence of α on frequency depicts that Ni/SnO_2-200 sample shows the biggest α values in the frequency range of 1-18 GHz. Therefore, it can be inferred that the Ni/SnO_2-200 sample may possesses better electromagnetic absorption properties than those of Ni/SnO_2-180 and Ni/SnO_2-220 samples.

To further evaluate the electromagnetic absorption properties of the as-synthesized Ni/SnO_2 samples, the reflection loss (RL) values of the Ni/SnO_2-200, Ni/SnO_2-180 and Ni/SnO_2-220 hybrid composites were simulated based on the measured complex permeability and permittivity for a given bsorber thickness and tested frequency, using the following equations:[56-58]

$$RL = 20\log_{10}\left|(Z_{in} - Z_0)/(Z_{in} + Z_0)\right| \quad (5)$$

$$Z_{in} = Z_0\sqrt{\frac{\mu_r}{\varepsilon_r}}\tanh\left(j\frac{2\pi fd\sqrt{\mu_r\varepsilon_r}}{c}\right) \quad (6)$$

where Z_0 is the impedance of free space, Z_{in} is the input characteristic impedance, ε_r is the complex permittivity, μ_r is the complex permeability, f is the frequency, c is the velocity of light, and d is the absorber thickness. Fig. 9(a) depicts the calculated reflection loss (RL) curves of Ni microspheres and Ni/SnO_2 hybrid composites with an absorber thickness of 1.7 mm. It can be observed that the microwave absorption performances of Ni/SnO_2 hybrid composites are superior to those of Ni microspheres. Especially for the Ni/SnO_2-200 sample, it exhibits the best electromagnetic absorption properties. The optimal reflection loss of -36.7dB was observed at 12.3 GHz and RL values below -10 dB (90% microwave absorption) were obtained in the 10.6-14.0 GHz rang with absorber thickness of only 1.7 mm. In our earlier literature,[59] the solid Ni/SnO_2 hybrids were successfully prepared and their minimal reflection loss as low as -21.7 dB was obtained at 8.6 GHz with the thickness of 3 mm. Compared with solid Ni/SnO_2 hybrids, the electromagnetic absorption properties of porous hollow Ni/SnO_2 composites were largely improved. The optimal reflection loss of -36.7dB was obtained at 12.3 GHz with absorber thickness of only 1.7 mm**.** It is well known the thickness of the sample is one of the key parameters and determines the position and the intensity of the frequency at the reflection loss minimum. Fig.S4 exhibits the simulated reflection loss of Ni microspheres with various thicknesses. It can be observed that the Ni sample shows weak electromagnetic absorption properties. The minimum reflection loss is only -6.2 dB at 12.3 GHz with absorber thickness of 2.5 mm. The calculated RL curves of Ni/SnO_2-180, Ni/SnO_2-200 and Ni/SnO_2-220 samples with different thicknesses are shown in

Fig.9(b–d). Notably, one can found that the absorption peaks mover to the high frequency with the decreasing thickness of the composites, which can be explained by the expression of $d = n\lambda/4$ (n=1, 3, 5, 7, 9, ...) in which the incident and reflected waves in the absorber are out of phase 180°, which results in the reflected waves in the air-absorber interface totally canceled. [60, 61] Meanwhile, among the three Ni/SnO_2 hybrid samples, Ni/SnO_2-200 sample exhibits the greatest electromagnetic absorption properties (Fig.9c). The minimal RL of -36.7 dB was observed at 12.3 GHz and bandwidth of RL values below -10 dB (90% microwave dissipation) can be tuned between 5.0 and 16.0 GHz in the absorber thickness of 1.5-3.5 mm. Table 1 shows the microwave absorption properties of typical Ni-based composites and other hybrid composites. [11-19, 24, 58] It can be seen that the porous hollow Ni/SnO_2 hybrids show stronger electromagnetic absorption properties, which also possess the advantages of thinner absorber thickness and broader absorption bandwidth.

Table 1 Microwave absorption properties of some reported Ni-based composites and other hybrid composites

Sample	Minimum RL value (dB)	Matching thickness (mm)	Matching frequency (GHz)	Frequency range (RL<-10 dB) (GHz)	Ref.
Octahedral Ni	–40.44	2.5	8.8	7.1–11.2	[11]
Ni fiber	–39.5	3.0	4.8	6.6–8.8	[12]
Ni chains	–19.9	0.8	17.2	15.7–18.0	[13]
Ni/SnO_2	–18.6	7.0	14.7	13.8–15.3	[14]
Carbon-coated nickel	–32	2.0	13.0	11.2–15.5	[15]
PS@PPy@Ni	–20.06	2.0	10.69	9.16–13.75	[16]
Ni/Polypyrrole	–15.2	2.0	13.0	11–15.4	[17]
Ni/polyaniline	–35	5.0	17.2	4.9–6.1 16.2–18	[18]
Ni/ZnS	–20.06	2.7	14.24	11.52–16.24	[19]
Fe_3O_4/SnO_2 core/shell nanorods	– 27.38	4.0	16.72	3.8–5.1 16.2–17.4	[24]
Fe_3O_4/basalt fibers	–31.1	5.0	5.9	5.3–6.5	[58]
Hollow porous Ni/SnO_2	–36.7	1.7	12.3	10.6–14.0	present work

Based on the above analysis, impedance match and electromagnetic wave attenuation are two vital factors that make contribution to the electromagnetic wave absorption properties. In this work, combing dielectric loss of SnO_2 with magnetic loss of Ni the synergistic effect is favorable for microwave absorption. Otherwise, the heterogeneous interfacial polarization in the hybrids can also promote dissipation of microwave energy.[62] Besides these, the hollow porous Ni/SnO_2 structure can provide more active sites for reflection and scattering of electromagnetic waves.[63] As shown in Fig.10, when the sample was placed under the radiation of electromagnetic wave, Due to the hollow structure, the microwaves can penetrate through Ni skeletons or SnO_2 nanoparticles deposited on the Ni shells, which allow the microwaves enter into interior void parts. The incident electromagnetic waves entering the hollow structure could be repeatedly reflected and scattered, and they were hard to escape from these porous hollow structure until being dissipated as heat. Otherwise, the porous hollow Ni possess pores with different sizes, which could be considered to be ‘‘defects’’. The presence of many pores in hollow Ni could provide another additional pathway for the absorption of electromagnetic wave.[64-66]

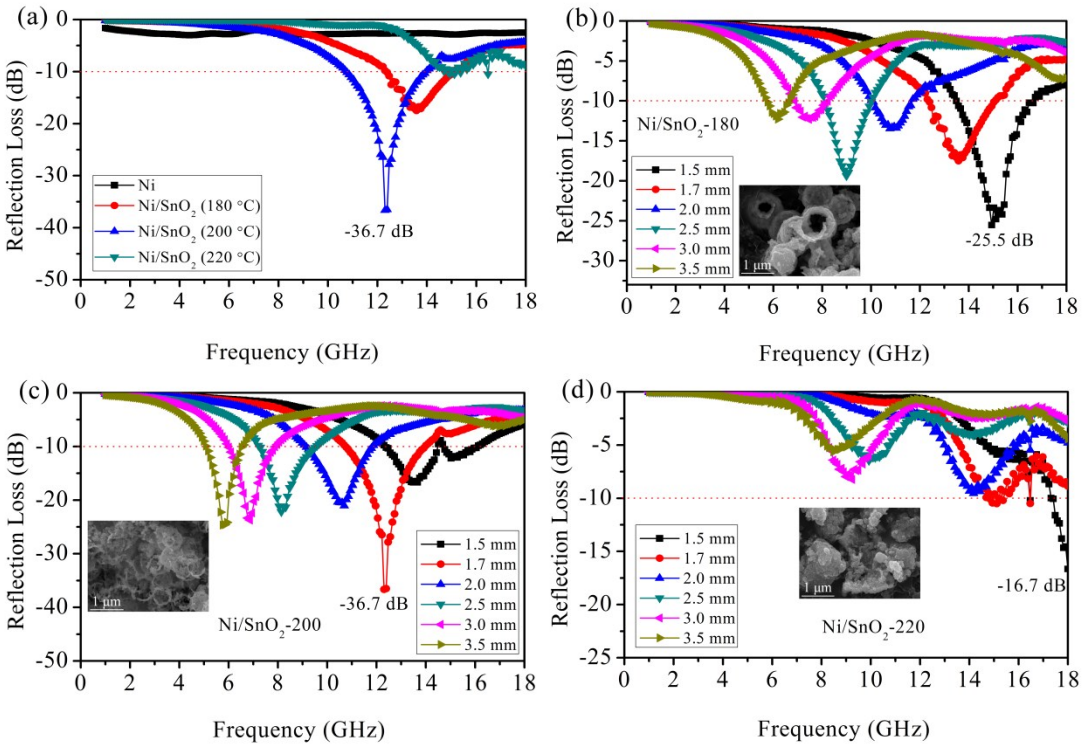

Fig. 9 The calculated reflection losses of comparison of electromagnetic wave reflection losses of the pristine Ni microspheres and three Ni/SnO_2 hybrid samples with a thickness of 1.7 mm; The simulated reflection loss of (b) Ni/SnO_2-180, (c) Ni/SnO_2-200 and (d) Ni/SnO_2-220 samples with various thicknesses.

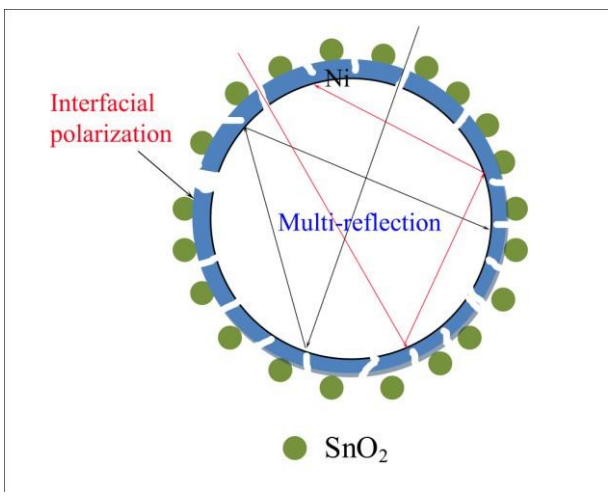

Fig. 10 Schematic presentation of possible microwave absorbing mechanisms in the hollow porous Ni/SnO_2 composites

4. Conclusion

In summary, the novel hybrids based on SnO_2 nanoparticles decorated on the hollow porous Ni skeletons were prepared through a two-step method by assistance of reaction-induced acid corrosion. These hollow porous Ni/SnO_2 hybrids can be used as lightweight, highly efficient absorbents in microwave absorbing materials at diverse working frequencies. In our protocol, the reaction temperature had a strong effect on the morphologies and phases of the resultant products. A plausible mechanism of formation hollow porous Ni/SnO_2 hybrids was proposed based on the chemical conversion-induced acid etching. In comparison with pristine Ni microspheres, the Ni/SnO_2 hybrid composites exhibit better microwave absorption capabilities. The minimum reflection loss of Ni/SnO_2-200 sample prepared at 200°C was −36.7 dB at 12.3 GHz. Moreover, the effective bandwidth (RL< -10 dB, 90% microwave absorption) can be tuned in the 5.0 -16.0 GHz with absorber thickness of 1.5-3.5 mm. The outstanding microwave absorption properties are attributed to good impedance match, multiple reflection, interfacial polarization and unique hollow porous structure. As a result, the as-synthesized hollow porous Ni/SnO_2 hybrid composites have a wide absorption frequency range, strong absorption ability, thin-

thickness and light-weight, which are very attractive for potential applications in electromagnetic wave absorbing materials.

Acknowledgements

This work was supported by the National Natural Science Foundation of China (Grant No. 51172213).

Notes and references

[a] *School of Materials Science and Engineering, Zhengzhou University, Zhengzhou 450001, China*

[b] *Zhengzhou Institute of Aeronautical Industry Management, Zhengzhou 450046, China*

** Corresponding Author.*

Dr. Gang Shao

E-mail address: gang_shao@zzu.edu.cn

Prof. Rui Zhang

Tel: +86-371-60632007

Fax: +86-371-60632600

E-mail address: zhangray@zzu.edu.cn

1. J. Zhu, S. Wei, N. Haldolaarachchige, D. P. Young and Z. Guo, *J. Phys. Chem. C*, 2011, **115**, 15304-15310.
2. L. Kong, X. Yin, Y. Zhang, X. Yuan, Q. Li, F. Ye, L. Cheng and L. Zhang, *J. Phys. Chem. C*, 2013, **117**, 19701-19711.
3. M. Mishra, A. P. Singh, B. P. Singh, V. N. Singh and S. K. Dhawan, *J. Mater. Chem. A*, 2014, **2**, 13159-13168.
4. Y. Zhang, Y. Huang, T. Zhang, H. Chang, P. Xiao, H. Chen, Z. Huang and Y. Chen, *Adv. Mater.*, 2015, **27**, 2049-2053.
5. Y.-L. Ren, H.-Y. Wu, M.-M. Lu, Y.-J. Chen, C.-L. Zhu, P. Gao, M.-S. Cao, C.-Y. Li and Q.-Y. Ouyang, *ACS Appl. Mater. Interfaces*, 2012, **4**, 6436-6442.
6. S.-T. Hsiao, C.-C. M. Ma, W.-H. Liao, Y.-S. Wang, S.-M. Li, Y.-C. Huang, R.-B. Yang and W.-F. Liang, *ACS Appl. Mater. Interfaces*, 2014, **6**, 10667-10678.
7. D. Sun, Q. Zou, Y. Wang, Y. Wang, W. Jiang and F. Li, *Nanoscale*, 2014, **6**, 6557-6562.
8. H. R. Tantawy, D. E. Aston, J. R. Smith and J. L. Young, *ACS Appl. Mater. Interfaces*, 2013, **5**, 4648-4658.
9. G. Sun, B. Dong, M. Cao, B. Wei and C. Hu, *Chem. Mater.*, 2011, **23**, 1587-1593.
10. J. Jiang, D. Li, D. Geng, J. An, J. He, W. Liu and Z. Zhang, *Nanoscale*, 2014, **6**, 3967-3971.
11. G. Tong, Q. Hu, W. Wu, W. Li, H. Qian and Y. Liang, *J. Mater. Chem.*, 2012, **22**, 17494-17504.
12. C. Gong, J. Zhang, X. Zhang, L. Yu, P. Zhang, Z. Wu and Z. Zhang, *J. Phys. Chem. C*, 2010, **114**, 10101-10107.
13. B. Zhao, B. Fan, G. Shao, B. Wang, X. Pian, W. Li and R. Zhang, *Appl. Surf. Sci.*, 2014, **307**, 293-300.
14. B. Zhao, G. Shao, B. Fan, W. Li, X. Pian and R. Zhang, *Mater. Lett.*, 2014, **121**, 118-121.
15. X. F. Zhang, X. L. Dong, H. Huang, Y. Y. Liu, W. N. Wang, X. G. Zhu, B. Lv, J. P. Lei and C. G. Lee, *Appl. Phys. Lett.*, 2006, **89**, 053115.
16. W. Li, T. Qiu, L. Wang, S. Ren, J. Zhang, L. He and X. Li, *ACS Appl. Mater. Interfaces*, 2012, **5**, 883-891.
17. P. Xu, X. Han, C. Wang, D. Zhou, Z. Lv, A. Wen, X. Wang and B. Zhang, *J. Phys. Chem. B*, 2008, **112**, 10443-10448.
18. X. L. Dong, X. F. Zhang, H. Huang and F. Zuo, *Appl. Phys. Lett.*, 2008, **92**, 013127.
19. B. Zhao, G. Shao, B. Fan, W. Zhao, Y. Xie and R. Zhang, *RSC Adv.*, 2014, **4**, 61219-61225.
20. W. Zhou, C. Cheng, J. Liu, Y. Y. Tay, J. Jiang, X. Jia, J. Zhang, H. Gong, H. H. Hng, T. Yu and H. J. Fan, *Adv. Funct. Mater.*, 2011, **21**, 2439-2445.
21. P. Sun, W. Zhao, Y. Cao, Y. Guan, Y. Sun and G. Lu, *CrystEngComm*, 2011, **13**, 3718-3724.
22. X. W. Lou, Y. Wang, C. Yuan, J. Y. Lee and L. A. Archer, *Adv. Mater.*, 2006, **18**, 2325-2329.
23. H. Wang and A. L. Rogach, *Chem. Mater.*, 2013, **26**, 123-133.

24. Y.-J. Chen, P. Gao, R.-X. Wang, C.-L. Zhu, L.-J. Wang, M.-S. Cao and H.-B. Jin, *J. Phys. Chem. C*, 2009, **113**, 10061-10064.
25. J. Liu, J. Cheng, R. Che, J. Xu, M. Liu and Z. Liu, *J. Phys. Chem. C*, 2012, **117**, 489-495.
26. M. Mishra, A. P. Singh, B. P. Singh and S. K. Dhawan, *RSC Adv.*, 2014, **4**, 25904-25911.
27. B. Zhao, G. Shao, B. Fan, W. Guo, Y. Chen and R. Zhang, *Appl. Surf. Sci.*, 2015, **332**, 112-120.
28. M. Epifani, M. Alvisi, L. Mirenghi, G. Leo, P. Siciliano and L. Vasanelli, *J. Am. Ceram. Soc.*, 2001, **84**, 48-54
29. I. u. Haq and T. I. Khan, *Surf. Coat. Technol.*, 2011, **205**, 2871-2875..
30. N. Lavanya, S. Radhakrishnan and C. Sekar, *Biosens. Bioelectron.*, 2012, **36**, 41-47
31. B. Zhao, G. Shao, B. Fan, C. Wang, Y. Xie and R. Zhang, *Powder Technol.*, 2015, **270,** 20-26.
32. B. Zhao, G. Shao, B. Fan, W. Zhao and R. Zhang, *RSC Adv.*, 2014, **4**, 57424-57429.
33. J.-X. Cui, W.-S. Wang, L. Zhen, W.-Z. Shao and Z.-L. Chen, *CrystEngComm*, 2012, **14**, 7025-7030.
34. Y. Zhao, F. Pan, H. Li, D. Zhao, L. Liu, G. Q. Xu and W. Chen, *J. Phys. Chem. C*, 2013, **117**, 21718-21723.
35. X. M. Yin, C. C. Li, M. Zhang, Q. Y. Hao, S. Liu, L. B. Chen and T. H. Wang, *J. Phys. Chem. C*, 2010, **114**, 8084-8088.
36. A. Wang, W. Wang, C. Long, W. Li, J. Guan, H. Gu and G. Xu, *J. Mater. Chem. C*, 2014, **2**, 3769-3776.
37. L. Wang, X. Jia, Y. Li, F. Yang, L. Zhang, L. Liu, X. Ren and H. Yang, *J. Mater. Chem. A*, 2014, **2**, 14940-14946.
38. H. Li, Y. Huang, G. Sun, X. Yan, Y. Yang, J. Wang and Y. Zhang, *J. Phys. Chem. C*, 2010, **114**, 10088-10091.
39. X.-L. Shi, M.-S. Cao, J. Yuan, Q.-L. Zhao, Y.-Q. Kang, X.-Y. Fang and Y.-J. Chen, *Appl. Phys. Lett.*, 2008, **93**, 183118.
40. X. Liu, D. Geng, H. Meng, P. Shang and Z. Zhang, *Appl. Phys. Lett.*, 2008, **92**, 173117
41. P. Xu, X. Han, C. Wang, D. Zhou, Z. Lv, A. Wen, X. Wang and B. Zhang, *J. Phys. Chem. B*, 2008, **112**, 10443-10448.
42. G. Tong, J. Yuan, W. Wu, Q. Hu, H. Qian, L. Li and J. Shen, *CrystEngComm*, 2012, **14**, 2071-2079.
43. Y. Ren, C. Zhu, S. Zhang, C. Li, Y. Chen, P. Gao, P. Yang and Q. Ouyang, *Nanoscale*, 2013, **5**, 12296-12303.
44. T. Chen, F. Deng, J. Zhu, C. Chen, G. Sun, S. Ma and X. Yang, *J. Mater. Chem.*, 2012, **22**, 15190-15197.
45. P. Toneguzzo, O. Acher, G. Viau, F. Fiévet-Vincent and F. Fiévet, *J. Appl. Phys.*, 1997, **81**, 5546-5548.
46. A. Aharoni, *J. Appl. Phys.*, 1991, **69**, 7762-7764.
47. Y. Lü, Y. Wang, H. Li, Y. Lin, Z. Jiang, Z. Xie, Q. Kuang and L. Zheng, *ACS Appl. Mater. Interfaces*, 2015, **7**, 13604-13611.
48. C. He, S. Qiu, X. Wang, J. Liu, L. Luan, W. Liu, M. Itoh and K.-i. Machida, *J. Mater. Chem.*, 2012, **22**, 22160-22166**.**
49. X. Sun, J. He, G. Li, J. Tang, T. Wang, Y. Guo and H. Xue, *J. Mater. Chem. C*, 2013, **1**, 765-777.
50. H. Yu, T. Wang, B. Wen, M. Lu, Z. Xu, C. Zhu, Y. Chen, X. Xue, C. Sun and M. Cao, *J. Mater. Chem*, 2012, **22**, 21679-21685.
51. B. Zhao, G. Shao, B. Fan, B. Sun, K. Guan and R. Zhang, *J. Mater. Sci.: Mater. Electron.*, 2014, **25**, 3614-3621.
52. P. H. Fang, *J. Chem. Phys.*, 1965, **42**, 3411-3413.
53. Y. Du, T. Liu, B. Yu, H. Gao, P. Xu, J. Wang, X. Wang and X. Han, *Mater. Chem. Phys.*, 2012, **135**, 884-891.
54. J. Xiang, J. Li, X. Zhang, Q. Ye, J. Xu and X. Shen, *J. Mater. Chem. A*, 2014, **2**, 16905-16914.
55. S. L. Wen, Y. Liu, X. C. Zhao, J. W. Cheng and H. Li, *Phys. Chem. Chem. Phys.*, 2014, **16**, 18333-18340.

56. G. Wang, Z. Gao, S. Tang, C. Chen, F. Duan, S. Zhao, S. Lin, Y. Feng, L. Zhou and Y. Qin, *ACS Nano*, 2012, **6**, 11009-11017.

57. F. Wang, J. Liu, J. Kong, Z. Zhang, X. Wang, M. Itoh and K.-i. Machida, *J. Mater. Chem.*, 2011, **21**, 4314-4320.

58. H. Guo, Y. Zhan, Z. Chen, F. Meng, J. Wei and X. Liu, *J. Mater. Chem. A*, 2013, **1**, 2286-2296.

59. B. Zhao, G. Shao, B. Fan, W. Zhao and R. Zhang, *J. Mater. Sci.: Mater. Electron.*, 2015, **26**, 5393-5399.

60. C. Wang, X. Han, X. Zhang, S. Hu, T. Zhang, J. Wang, Y. Du, X. Wang and P. Xu, *J. Phys. Chem. C*, 2010, **114**, 14826-14830.

61. A. N. Yusoff, M. H. Abdullah, S. H. Ahmad, S. F. Jusoh, A. A. Mansor and S. A. A. Hamid, *J. Appl. Phys.*, 2002, **92**, 876-882.

62. Y.-J. Chen, F. Zhang, G.-g. Zhao, X.-y. Fang, H.-B. Jin, P. Gao, C.-L. Zhu, M.-S. Cao and G. Xiao, *J. Phys. Chem. C*, 2010, **114**, 9239-9244.

63. R. Pang, X. Hu, S. Zhou, C. Sun, J. Yan, X. Sun, S. Xiao and P. Chen, *Chem. Commun.*, 2014, **50**, 12493-12496.

64. B. Zhao, G. Shao, B. Fan, Y. Xie, B. Sun and R. Zhang, *Adv. Powder Technol.*, 2014, **25**, 1761-1766.

65. G. Li, T. Xie, S. Yang, J. Jin and J. Jiang, *J. Phys. Chem. C*, 2012, **116**, 9196-9201.

66. Y. Huang, Y. Wang, Z. Li, Z. Yang, C. Shen and C. He, *J. Phys. Chem. C*, 2014, **118**, 26027-26032.